JACS
JOURNAL OF THE AMERICAN CHEMICAL SOCIETY

pubs.acs.org/JACS Article

Site-Specific Carbonylation of Dimethoxymethane over Brønsted Acids in the Opened Sodalite Cages of FAU Zeolite

Youming Ni,[#] Xingwang Gong,[#] Wenna Zhang,[#] Hua Li, Yingying Sheng, Shutao Xu,* Yingxu Wei, Wenliang Zhu,* and Zhongmin Liu

Cite This: J. Am. Chem. Soc. 2025, 147, 44950−44961 Read Online

ACCESS | Metrics & More | Article Recommendations | Supporting Information

ABSTRACT: Methyl methoxyacetate (MMAc) is a valuable platform molecule used in biodegradable polymers, polyester fibers, and fine chemicals. While zeolite-catalyzed carbonylation of dimethoxymethane (DMM) to MMAc is a sustainable route, achieving high selectivity, stability, and efficiency simultaneously remains challenging. Herein we demonstrate that strategically opening sodalite (SOD) cages within FAU-type zeolites creates optimal Brønsted acid microenvironments for DMM carbonylation. An H-FAU-I-F zeolite (Si/Al ≈ 6), prepared via mild NH_4F treatment to open SOD cages, maintained 90% MMAc selectivity and a space-time yield of 0.7 $g{\cdot}g^{-1}{\cdot}h^{-1}$ over 500 h of continuous operation—representing unprecedented catalytic activity and stability. Solid-state NMR studies (using ^{2}H-DMM and ^{13}CO) revealed preferential enrichment of DMM and CO within the opened SOD cages. In situ $^1H-^{13}C$ CP MAS NMR directly captured the insertion of CO into DMM occurring specifically in SOD nanoreactors. DFT calculations attributed their superior activity to enhanced acid strength and transition-state stabilization. This work establishes a cage-engineering strategy for designing efficient and durable industrial carbonylation catalysts.

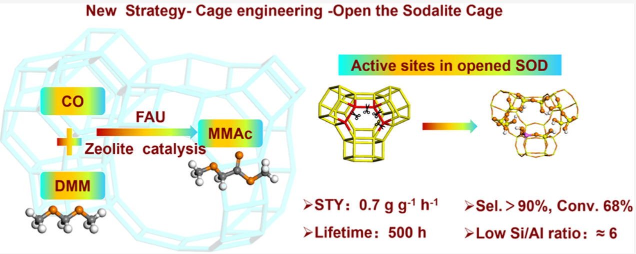

INTRODUCTION

Fossil energy shortages, global warming, air pollution, and the accumulation of plastic waste are severe issues today that endanger human health and restrict the sustainable development of society.[1,2] The catalytic transformation of renewable feedstocks (biomass, solar, wind) and CO_2-derived platform molecules (H_2, CO, methanol) into value-added chemicals, biodegradable polymers, and clean fuels presents a promising circular economy solution.[3] Among these strategic intermediates, methyl methoxyacetate (MMAc) emerges as a versatile molecular building block with multifaceted applications in sustainable industrial processes. As shown in Scheme 1, first and foremost, MMAc serves as a critical precursor for ethylene glycol (monomer) production via catalytic hydrogenation and hydrolysis, which is a cornerstone compound in polyester fiber manufacturing.[4] Furthermore, its utility extends to clean fuel technology as an advanced oxygenated additive, demonstrated to significantly reduce NO_x emissions (27−35%) and particulate matter formation while enhancing fuel stability at low temperatures.[5] Notably, the molecular architecture of MMAc, featuring synergistic functional groups including ester, ether, and reactive α-hydrogen moieties, enables its conversion into high-value fine chemicals and bioactive compounds through selective catalysis.[6] Of particular environmental significance, MMAc hydrolysis derivatives (methyl glycolate and glycolic acid) provide a green pathway to polyglycolic acid (PGA) synthesis.[7] This biopolymer exhibits exceptional mechanical strength and gas barrier properties, making it ideal for high-performance applications from deep-well drilling tools to food packaging.[8] Remarkably, PGA demonstrates complete enzymatic biodegradation into CO_2 and H_2O, addressing critical plastic waste concerns. At present, the technology of preparing methyl glycolate based on dimethoxymethane (DMM) carbonylation has been developed by the Dalian Institute of Chemical Physics (DICP) and will be industrialized. This represents a new, groundbreaking technical route for the green development of the coal chemical industry.[7] This innovation signifies a paradigm shift in sustainable coal chemical utilization, integrating conventional fossil resources with green chemistry applications. In view of the expanding application landscape of MMAc and the urgent need for carbon-neutral technologies, the development of efficient catalytic systems for its synthesis from renewable resources remains a research priority of scientific and industrial importance.

Catalytic carbonylation of DMM over solid acid catalysts has been identified as an atom-economical pathway for MMAc

Received: August 1, 2025
Revised: November 18, 2025
Accepted: November 19, 2025
Published: November 29, 2025

https://doi.org/10.1021/jacs.5c13217

Scheme 1. Synthesis Route of MMAc from DMM and Its Applications

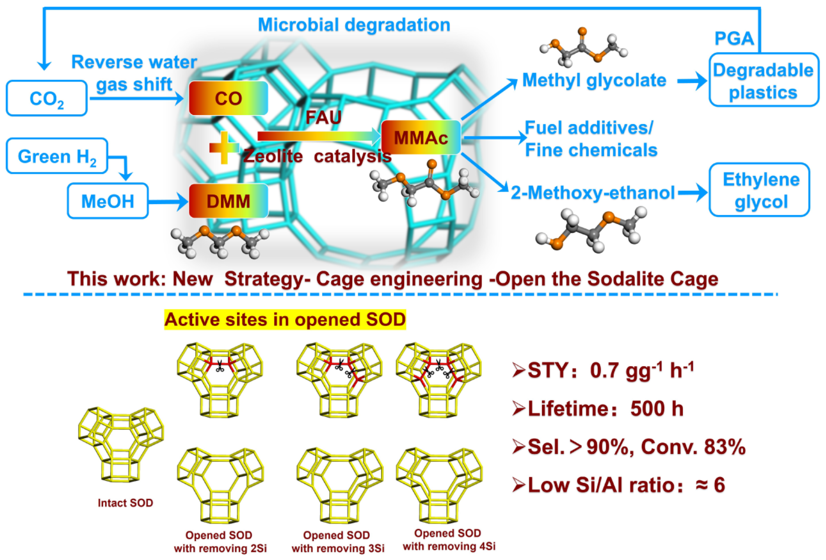

synthesis, leveraging established industrial processes for DMM production from methanol.[9−13] This Koch-type carbonylation mechanism shares fundamental similarities with dimethyl ether (DME) carbonylation systems.[14−16] However, DMM's poor stability on acidic catalysts renders it prone to disproportionation into DME and methyl formate (MF), resulting in a low MMAc selectivity. A pioneering work by the Alexis T. Bell group reported that 79% MMAc selectivity was achieved in DMM carbonylation over H-FAU zeolite with a high Si/Al ratio (Si/Al = 30) merely at 373 K.[17] They considered the low Brønsted acid density of the high Si/Al H-FAU zeolites would be beneficial in terms of enlarging the spacing of surface methoxy species, which weakens their electrostatic repulsion and lowers the activation energy for CO insertion.[18,19] The H-FAU zeolite features a three-dimensional microporous framework including supercages (SC, 1.12 nm diameter) interconnected through 12-membered ring apertures (0.74 nm) and sodalite cages (SOD, 0.63 nm) accessible only via six-membered ring windows (0.25 nm). Interestingly, recent reports suggest that previously inaccessible Brønsted acids in SOD can be unlocked after desilication or dealumination of FAU zeolites, thereby enhancing the catalytic activities.[20−22] This phenomenon aligns with established knowledge that acid sites in a confined zeolite environment exhibit extraordinary catalytic activity when accessible. For instance, confined Brønsted acids in the 8-membered ring (8-MR) side pockets of mordenite rather than in the larger 12-MR channels have been confirmed to be the key catalytic sites for DME carbonylation.[15,16] Given that SOD is sufficiently large to accommodate DMM and MMAc molecules, yet narrower than SC, it can be hypothesized that the Brønsted acids contained within opened SOD cages may also be instrumental in the carbonylation of DMM. Furthermore, recent studies have indicated that an increase in DMM conversion invariably leads to a reduction in selectivity due to intensified disproportionation, which decomposes DMM into formaldehyde intermediates.[23,24] Increased aldehyde species on the surface of zeolites accelerate coke formation and catalyst deactivation. Consequently, in pursuit of high activity in DMM carbonylation catalysts, durability warrants equal consideration.

In this work, through an integrated experimental-theoretical approach, we systematically deciphered the structure−activity relationship in DMM carbonylation. Advanced solid-state NMR techniques ($^1H-^{13}C$ CP/MAS, HP ^{129}Xe NMR) in conjunction with DFT calculations conclusively demonstrated that opened SOD cages in H-FAU zeolites (Figure S1) function as nanoreactors for selective carbonylation. Moreover, the catalyst achieves a 90% stable MMAc selectivity with a space-time yield (STY) of 0.7 g g^{-1} h^{-1} over 500 h at 343 K on a SOD-opened H-FAU zeolite (Si/Al ≈ 6), thereby demonstrating its strong potential for industrial application.

RESULTS AND DISCUSSION

Catalytic Performance for DMM Carbonylation. The DMM carbonylation performances of various H-FAU zeolite catalysts were compared at 343 K, 1.0 MPa and a CO/DMM molar ratio of 19 (Figure 1a). The commercial H-FAU-I catalyst (Si/Al ≈ 5) exhibits moderate catalytic activity with 13.5% DMM conversion and 77.3% MMAc selectivity, accompanied by 13.8% DME and 7.4% MF byproduct formation from disproportionation reactions. Notably, the STY of MMAc remained merely at 0.11 g g^{-1} h^{-1}. After treatment with 10% NH_4F aqueous solution at 278 K for 5 min, the resulting H-FAU-I-F catalyst (Si/Al ≈ 6) showed significantly enhanced reactivity: DMM conversion and MMAc selectivity reached 40.3% and 82.9%, respectively, with the STY of MMAc as high as 0.37 g g^{-1} h^{-1}. Similar improvement was observed for H-FAU-II-F (Si/Al ≈ 4) versus parent H-FAU-II (Si/Al ≈ 3), where MMAc selectivityincreased noticeably and STY more than tripled. Temperature-dependent studies (Figure 1b) revealed superior low-temperature activity of the modified catalysts. At 333 K, H-FAU-I-F outperformed unmodified H-FAU-I at 358 K, achieving 25.2% DMM conversion and 85.1% MMAc selectivity. Parallel observations with the H-FAU-II series (Figure S2) confirmed the general efficacy of NH_4F treatment in boosting low-temperature activity. Product evolution for H-FAU-I at 333 K and 1.0 MPa (Figure 1c) showed an 18-h induction period dominated by DME/MF formation (<2% conversion), followed by rapid activation to 4.6% conversion and 70.1% MMAc selectivity at 26 h. This activation correlated with Brønsted acid-mediated

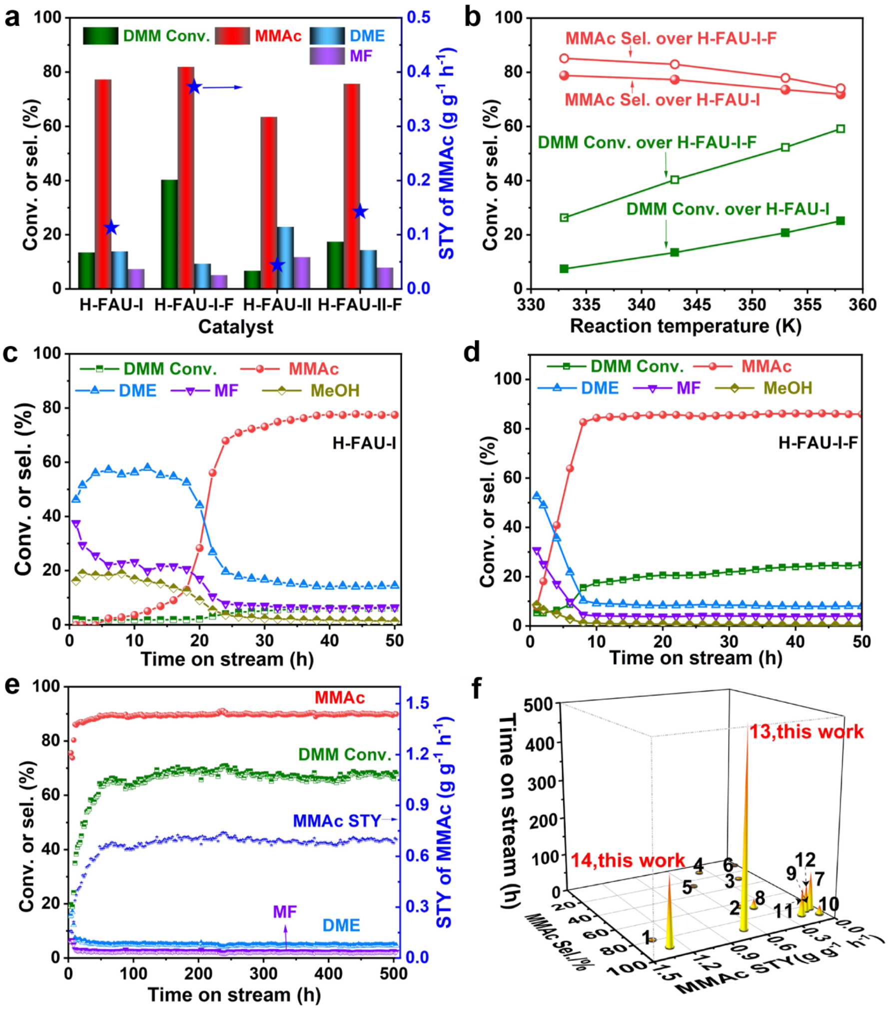

Figure 1. The catalytic performances of DMM carbonylation. (a) Catalytic activity comparisons over H-FAU catalysts at 343 K. (b) Effect of reaction temperatures on the catalytic results over H-FAU-I and H-FAU-I-F. (c) Evolution of the products over H-FAU-I at 333 K. (d) The evolution of the products over H-FAU-I-F at 333 K. (e) Stability test of H-FAU-I-F. (f) Comparison with the typical results concerning DMM carbonylation over zeolite catalysts in previous literatures. 1: H-FAU(30);[17] 2: H-FAU(15);[19] 3: H-MFI(13.5);[19] 4: H-MOR(10);[19] 5: H-BEA(12.5);[19] 6: H-FER(10);[19] 7: H-FAU(4.1);[12] 8: H-MFI(20);[13] 9: H-MOR(10.8);[25] 10: H-FAU(none);[26] 11: H-ZEO-1(21);[27] 12: H-FAU(30);[27] 13 and 14 (this work): H-FAU-I-F(6.4), and the numbers in parentheses indicate the Si/Al ratio. Note: for (a)−(d), catalyst mass = 0.5 g; reaction pressure = 1.0 MPa; CO = 40 mL/min at standard temperature and pressure (STP); and CO/DMM (molar ratio) = 19/1. For (e), catalyst mass = 1.0 g; reaction temperature = 343 K; reaction pressure = 5.0 MPa; CO = 80 mL/min at STP; and CO/DMM (molar ratio) = 19/1.

accumulation of surface methoxymethoxy species via the Koch mechanism.[4] Conversion and selectivity gradually increased to 6% and 77% by 50 h and were stabilized. Strikingly, H-FAU-I-F exhibited a sharply shortened induction period (Figure 1d), reaching 17.5% conversion and 84.4% selectivity at 10 h before stabilizing at ∼25% and 86% by 50 h. Consistent shortening was observed for H-FAU-II-F (Figures S3 and S4). The shorter induction period observed after NH_4F treatment may be attributed to the rapid removal by the initial product MMAc of detrimental species such as methanol and water from the DMM carbonylation reaction (Figure S5). Minor amounts of $CH_3O(CH_2O)_2CH_3$ (DMM_2) and its carbonylation products were detected (Figure S6). Long-term stability assessments demonstrated exceptional catalyst durability. At 343 K and 5.0 MPa (CO/DMM = 19), H-FAU-I-F maintained a stable performance (68% conversion, 90% selectivity, 0.7 g g^{-1} h^{-1} STY) for 500 h (Figure 1e). Characterization of the spent H-FAU-I-F catalyst revealed a light color and the absence of aromatic coke species, as determined by GC-MS analysis of retained substances (Figure S7). Only the residual MMAc product was detected, indicating almost no aromatic coke formation during the reaction. These results suggest that the H-FAU-I-F catalyst possesses significant potential for an extended operational lifetime. Under intensified conditions (353 K, 5.0 MPa, CO/DMM = 95), it achieved a record MMAc productivity with 90% selectivity and 1.3 g g^{-1} h^{-1} STY over 180 h (Figure S8). As benchmarked in Figure 1f and Table S1,[12,13,17,19,25,26,27] H-FAU-I-F surpasses reported zeolite catalysts in key metrics. First of all, reported zeolite catalysts exhibit an inferior low-temperature activity compared to H-FAU-I-F. For instance, Celik et al. reported below 5% DMM conversion at 363 K over H-FAU (Si/Al = 15 or 30).[17,19] Low-temperature operation enhances catalyst stability by suppressing high-temperature coking pathways (e.g., Prins, aldol, and hydroacylation reactions converting DMM to aromatics/coke).[23] Besides, H-FAU may be considered as the appropriate zeolite, notwithstanding, a very high Si/Al ratio (≥30) is required to achieve satisfactory reactivity.[17,19] This could lead

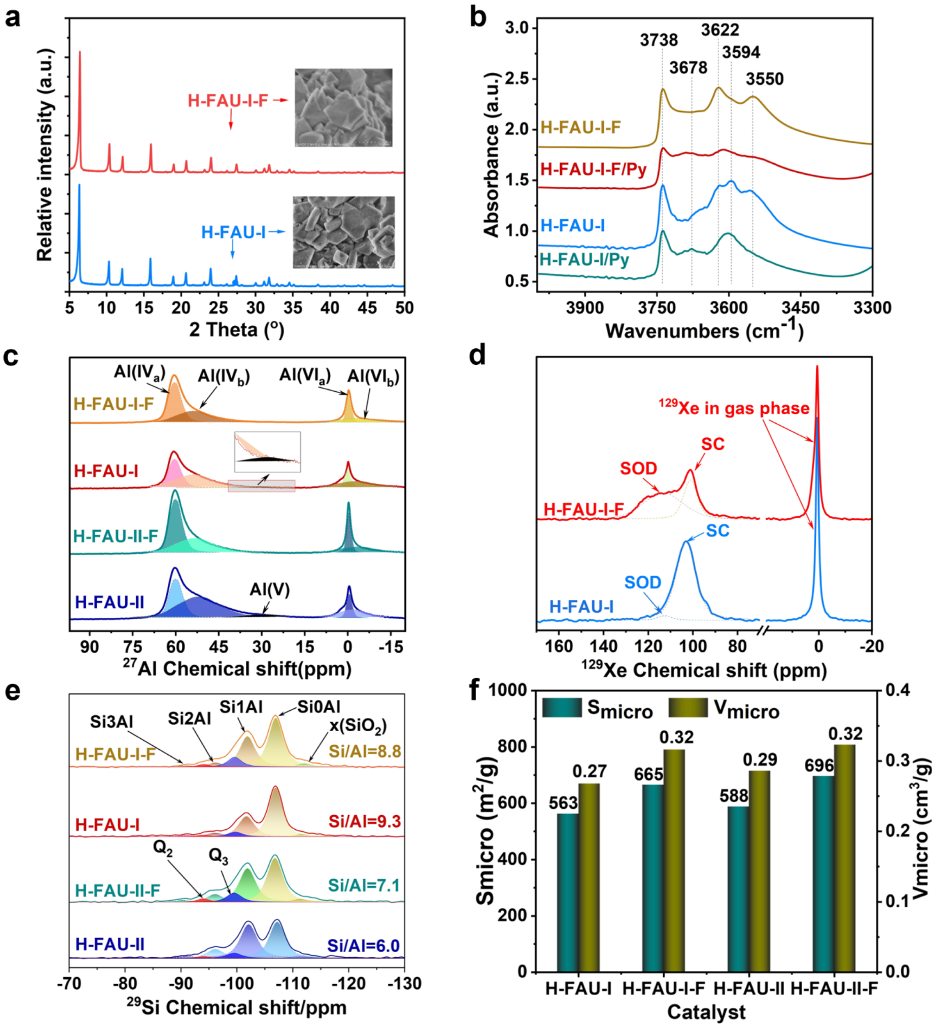

Figure 2. Structural characterizations of H-FAU zeolites. (a) XRD patterns and SEM images of H-FAU-I and H-FAU-I-F. (b) Infrared spectra of H-FAU-I and H-FAU-I-F before and after pyridine absorption at 523 K. (c) ^{27}Al MAS NMR spectra of H-FAU-I, H-FAU-I-F, H-FAU-II, and H-FAU-II-F. (d) HP ^{129}Xe NMR spectra of H-FAU-I and H-FAU-I-F at 193 K. (e) ^{29}Si MAS NMR spectra of H-FAU-I, H-FAU-I-F, H-FAU-II, and H-FAU-II-F. (f) Micropore surface area and volumes of H-FAU-I, H-FAU-I-F, H-FAU-II, and H-FAU-II-F by low-temperature nitrogen adsorption.

to high costs and pollution emissions, and deep dealumination is required for preparing high Si/Al H-FAU. Furthermore, MMAc STY for many selective catalysts falls below the industrial viability threshold of 0.2 g·g^{-1}·h^{-1} established for DME carbonylation processes. Collectively, the above analysis shows that high selectivity (>90%), exceptional STY (0.7−1.3 g·g^{-1}·h^{-1}), long-term stability (500 h), and moderate Si/Al ratio (6.4) make H-FAU-I-F promising for industrial application.

H-FAU Structural Characterizations. The structural integrity of NH$_4$F-modified catalysts is systematically verified through a multimodal characterization. XRD patterns and SEM micrographs (Figure 2a, Figure S9) reveal that mild NH$_4$F treatment preserves the crystallinity and morphological features of both H-FAU-I and H-FAU-II zeolites, indicating negligible structural degradation during modification. The infrared spectra in Figure 2b demonstrate that besides strong bands at 3550 (Brønsted acidic OH within SOD, B@SOD) and 3622 cm^{-1} (Brønsted acidic OH within SC, B@SC), bands at 3738 cm^{-1} (Silanol OH) and bands at 3678 and 3594 cm^{-1} (OH associated with extra-framework aluminum (EFAl)) are clearly detected for H-FAU-I.[21,22,28,29] The obvious existence of silanol OH and EFAl implies that the framework structure of commercial H-FAU-I was partially damaged during the preparation process. Compared to H-FAU-I, bands at 3678 and 3594 cm^{-1} for H-FAU-I-F are significantly reduced, which means that most of EFAl are eliminated through NH$_4$F modification. After pyridine adsorption for H-FAU-I or H-FAU-I-F, the bands at 3550 and 3622 cm^{-1} are substantially reduced, whereas the bands at 3678 and 3594 cm^{-1} are visibly preserved. The subtraction infrared spectra after pyridine adsorption (Figure S10) also illuminate these changes.

It indicates that pyridine can interact with B@SOD and B@SC, whereas the interaction between pyridine and EFAl is relatively weaker. The infrared spectra in Figure S9 also prove that the EFAl of H-FAU-II is effectively cleared by NH$_4$F, and the B@SOD and B@SC for both H-FAU-II and H-FAU-II-F are substantively shielded by pyridine. ^{27}Al MAS NMR is an effective method for identifying Al coordination and species in zeolites.[30−32] Five distinct Al species are resolved in the ^{27}Al MAS NMR spectra in Figure 2c. To fit these signals, the quadrupole coupling constant (C_Q) and asymmetry factor (η) are calculated from the ^{27}Al MQ MAS NMR spectra[32,33] (Figure S12 and Table S2). Deconvolution of the spectra indicates the presence of at least five Al species in the H-FAU zeolites: Al(IV$_a$) (~63 ppm, isotropic chemical shift), Al(IV$_b$) (~62 ppm), Al(V) (~40 ppm), Al(VI$_a$) (~1 ppm), and Al(VI$_b$) (~5 ppm). Al(IV$_a$) is attributed to framework tetrahedral aluminum (Al(IV)) sites, while Al(IV$_b$) characterized by higher C_Q values is assigned to framework Al(IV) in defective or distorted environments. Similarly, Al(VI) manifests as two distinct sites, which are Al(VI$_a$) with a symmetrical charge environment and Al(VI$_b$) with a higher C_Q value, respectively.[31] Similarly, Al(VI) can be resolved into two distinct sites: Al(VIa), characterized by a symmetrical charge environment, and Al(VIb), which exhibits a higher quadrupolar coupling constant (C_Q). Notably, NH_4F treatment significantly reduces the population of defective or distorted Al species while concurrently increasing the signal intensity at around 0 ppm. It is important to emphasize that framework and extra-framework aluminum species cannot be reliably distinguished solely on the basis of their chemical shifts in 1D ^{27}Al NMR spectra. For instance, several studies have demonstrated that the signal at 0 ppm disappears upon ammonium exchange, indicating that species previously assigned as extra-framework aluminum (EFAl) can be reincorporated into the zeolite framework under certain conditions.[34,35]

In a systematic review, Bokhoven et al. highlighted the complexity of aluminum speciation in zeolites.[36] They pointed out that tetrahedrally coordinated Al (resonating near 60 ppm) is not necessarily framework Al, nor is octahedrally coordinated Al (near 0 ppm) necessarily extra-framework Al; these species may interconvert under appropriate conditions.[36] Accordingly, they concluded that "counting all octahedral aluminum as EFAl is erroneous."

While the spectral identification of EFAl requires careful interpretation, it is well established that irreversible dealumination—occurring during ammonium exchange, ammonia desorption, and calcination—can lead to the formation of EFAl. Treatments such as with oxalic acid, $(NH_4)_2SiF_6$, or NH_4F are commonly employed to remove such EFAl species from zeolite surfaces[31,37−39] In our samples, NH_4F treatment effectively removed some distorted or defective Al species, leading to an overall improvement in the symmetry of the 1D ^{27}Al NMR spectra. Furthermore, quantitative ^{1}H NMR analysis revealed a reduction in the Al−OH groups, confirming the removal of certain EFAl species after treatment.

To further verify the assignment of the signal at 0 ppm, H-FAU-II and H-FAU-II-F were subjected to NH_4^+ exchange in 1 mol/L NH_4Cl solution for 2 h, after which ^{27}Al NMR spectra were reacquired (Figure S13). The disappearance of the signal at 0 ppm after exchange indicates that a substantial fraction of the corresponding Al species is framework-related and can be reversibly reincorporated. In contrast, certain species with large C_Q values did not revert to the framework after exchange, confirming that they are EFAl formed through irreversible dealumination. These latter species were effectively removed after NH_4F treatment, as evidenced by the disappearance of the corresponding broad spectral feature.

Complementary to aluminum characterization, hyperpolarized (HP) ^{129}Xe NMR is widely used to detect the zeolite channel connectivity at the molecular level at low temperatures.[20,40] Considering that the kinetic diameter of Xe (0.44 nm) exceeds the size of the 6-MR windows (0.25 nm), Xe adsorption into the SOD cages cannot be observed by ^{129}Xe NMR if the SOD cages remain intact. The signal at 0 ppm is attributed to the gas phase ^{129}Xe. As displayed in Figure 2d and Figure S14, H-FAU-I exhibits a single peak at about 103 ppm at 193 K, primarily assigned to Xe atoms confined within SC. Notably, H-FAU-I-F displays a broad peak at about 115 ppm, implying that Xe can access the SOD cages.[20,40] These HP ^{129}Xe NMR results demonstrate that NH_4F treatment enhances accessibility to the SOD cages.

The ^{1}H−^{1}H DQ-SQ NMR spectra effectively reveal the changes in correlations between hydroxyl species before and after NH_4F treatment; these correlated hydroxyl species will be discussed in detail in Figure S15. For H-FAU-I-F, the relevant signals only exhibit minor differences compared with those of H-FAU-I. The signal corresponding to the correlation between BAS in supercages and aluminum hydroxy disappears (3.70, 4.91) (1.21, 4.91), while a new correlation signal between aluminum hydroxy and BAS in the SOD cage emerges (4.53, 5.25) (0.72, 5.25). The ^{1}H NMR signals at 1.2 and 0.8 ppm are attributed to aluminum hydroxy, which were confirmed by ^{1}H−^{27}Al RESPDOR NMR experiments (Figure S16). The DQ results from the two samples revealed that the newly observed correlation signals between Al−OH and BAS@SOD might originate from the spatial proximity of newly generated Al−OH groups and BAS within opened SOD cages after NH_4F treatment, which also indicates that the SOD cages were opened.

As summarized in Table S3, the framework Si/Al ratio determined by ^{29}Si NMR (Figure 2e) is higher than the bulk Si/Al ratio from the XRF analysis. This indicates the effective removal of extra-framework aluminum (EFAl) species during NH_4F treatment. Furthermore, the framework Si/Al ratio remains largely unchanged before and after the treatment, which suggests that the NH_4F leaching process is relatively mild and does not cause significant extraction of framework silicon or aluminum. However, the number of Brønsted acidic sites quantified by Py-IR and ^{1}H NMR is prominently enhanced in the modified samples. This suggests that NH_4F treatment primarily removes EFAl with minimal damage to the H-FAU framework, leading to better exposure and proximity of Brønsted acidic sites. Theoretically, the N_2 molecule (kinetic diameter of 0.36 nm), which is larger than the 6-MR windows (0.25 nm), cannot access the SOD micropores. However, the micropore volumes determined from N_2 isotherms for the H-FAU-I-F and H-FAU-II-F are about 18% and 13% higher than those of H-FAU-I and H-FAU-II, respectively (Figure 2f and Table S3). This elevation is likely due to enhanced N_2 access to SOD micropores through opened 6-MR windows.[20] The apparent diffusion coefficients (D_{eff}) measured by the intelligent gravimetric analyzer (IGA) method are provided in Table S3, Figures S17 and S18. Paradoxically, the D_{eff} values of DMM and MMAc for the NH_4F-modified H-FAU are both slightly lowered, which is contrary to expectations. Previous studies suggested that the H-FAU zeolites with larger external specific surface areas and mesoporous volumes exhibited better reactivity due to mass transfer efficiency.[12] However, the IGA results explicitly do not support such a speculation. This discrepancy is likely attributable to the increased number of accessible Brønsted acidic sites within the opened SOD cages, which enhances the adsorption of DMM and MMAc. Consequently, despite the increases in the BET surface area and pore volume, they did not lead to significantly faster

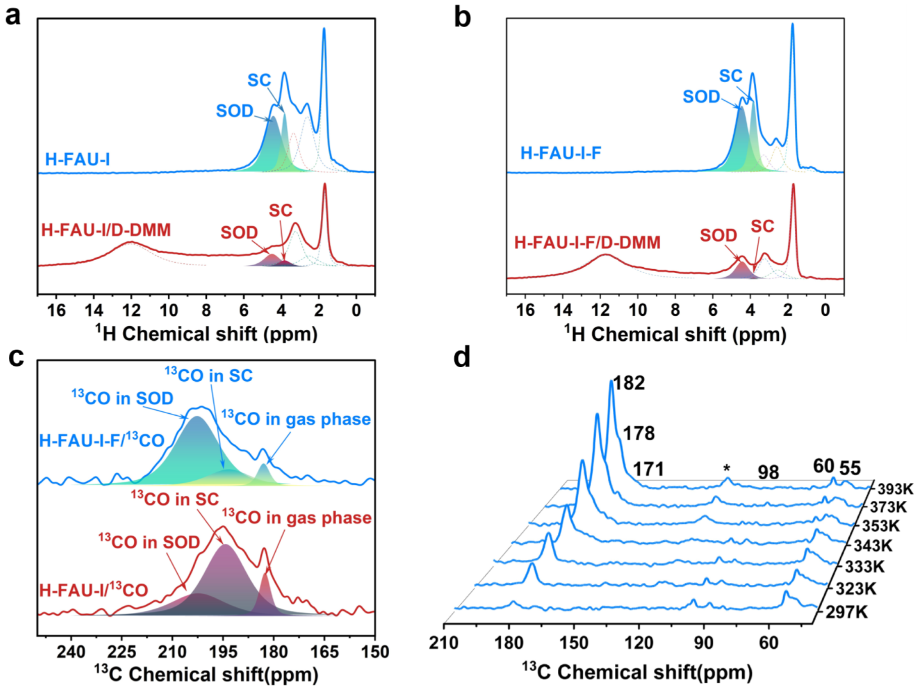

Figure 3. MAS NMR spectra of isotope labeled reactants adsorption and reaction on H-FAU zeolites. (a) and (b) ^{1}H MAS NMR spectra of ^{2}H-DMM adsorption on H-FAU-I and H-FAU-I-F, respectively. (c) ^{13}C MAS NMR spectra of ^{13}CO adsorbed in H-FAU-I and H-FAU-I-F zeolites; the pressure of ^{13}CO is 1 atm. (d) *In situ* ^{1}H−^{13}C CP MAS NMR spectra of the temperature-programmed reaction between DMM and ^{13}CO on H-FAU-I-F. The pressure of ^{13}CO is 3 atm, and the asterisk denotes spinning sideband.

diffusion of reactants and products. Moreover, the slight decrease in D_{eff} can be attributed to the increased accessibility of Brønsted acid sites. The actual reactant (DMM) and product (MMAc) molecules exhibit strong interactions with these acid sites. The D_{eff} values derived from IGA desorption curves effectively capture these strong interactions within the Brønsted-acid-rich micropores. After NH_4F treatment, the number of Brønsted acid sites in the zeolite increases, enhancing its adsorption capacity for both DMM and MMAc, which consequently leads to a reduction in the level of D_{eff}. Nevertheless, the fact that D_{eff} does not decrease by an order of magnitude indicates that the alteration in diffusion performance is not the primary factor responsible for the enhanced catalytic performance.

Catalytic Centers and Mechanism by MAS NMR Studies. The above multiple characterization results of probe molecules such as N_2, pyridine, and ^{129}Xe have strongly demonstrated that the accessibility of the SOD Brønsted acid sites is improved after NH_4F treatment. In order to directly reveal their involvement in DMM carbonylation, the adsorption and reaction of DMM in H-FAU and H-FAU-F zeolites were observed by ^{1}H and ^{13}C MAS NMR. First, ^{1}H MAS NMR spectra of dehydrated H-FAU-I and H-FAU-I-F were acquired and deconvoluted, as shown in Figure 3a,b. The concentrations of hydroxyl species at various chemical shifts were quantitatively determined by using adamantane as an external standard. Signals at 3.8 and 4.5 ppm are assigned to B@SC and B@SOD, respectively. Signals at 2.5 and 1.7 ppm correspond to Al−OH and Si−OH species, respectively.[41,42] An additional signal at 3.3 ppm is also assigned to another Al−OH species, as evidenced by ^{1}H−^{27}Al S-RESPDOR MAS NMR (Figure S16). As listed in Table S4, the concentration of B@SOD in H-FAU-I is approximately twice that of B@SC. After modification, the concentration of B@SC, B@SOD, and Si−OH species increases significantly, while Al−OH species decrease markedly. These ^{1}H MAS NMR results are consistent with the FTIR spectra results in Figure 2b. Next, ^{1}H MAS NMR spectra following DMM adsorption were recorded (Figure 3a,b and Table S4). Due to the proximity of the ^{1}H chemical shifts of DMM $-CH_3$ (3.3 ppm) and $-O-CH_2-O-$ (4.4 ppm) to those of B@SC (3.8 ppm) and B@SOD (4.5 ppm), spectral overlap occurs between ordinary DMM signals and Brønsted acid sites. To improve spectral resolution, deuterated DMM (^{2}H-DMM, 99.7% molar fraction and 98% ^{2}H isotope labeling) was synthesized via condensation of deuterated methanol and deuterated formaldehyde and subsequently adsorbed. Remarkably, upon introduction of ^{2}H-DMM into H-FAU-I or H-FAU-I-F, both B@SC and B@SOD signals were substantially attenuated. This confirms that DMM can access the opened 6-MR windows and interact with B@SOD. After adsorption of ^{2}H-DMM, new peaks appear in the low-field region (8−14 ppm), which are attributed to ^{2}H-DMM adsorbed on Brønsted acid or SiOH groups.

Since N_2 and Xe can access the opened SOD cages of H-FAU-I-F, CO, with a similar molecular size, may also enter these confined spaces. To acquire direct evidence, dehydrated H-FAU-I and H-FAU-I-F samples, preencapsulated in NMR rotors, were exposed to ^{13}CO. ^{13}C high-power proton decoupling (hpdec) MAS NMR spectra were then collected and deconvoluted to infer the approximate distribution of adsorbed ^{13}CO. As shown in Figure 3c, the peak at 183 ppm corresponds to gas phase ^{13}CO, whereas the peaks at about 202 and 193 ppm are attributed to ^{13}CO located within opened SOD and SC, respectively. Notably, the proportion of ^{13}CO within SOD cages increased significantly after modification (from 24.0% to 74.8%), demonstrating enhanced CO accessibility of the opened SOD cages in H-FAU-I-F compared to H-FAU-I. This trend aligns with the HP ^{129}Xe

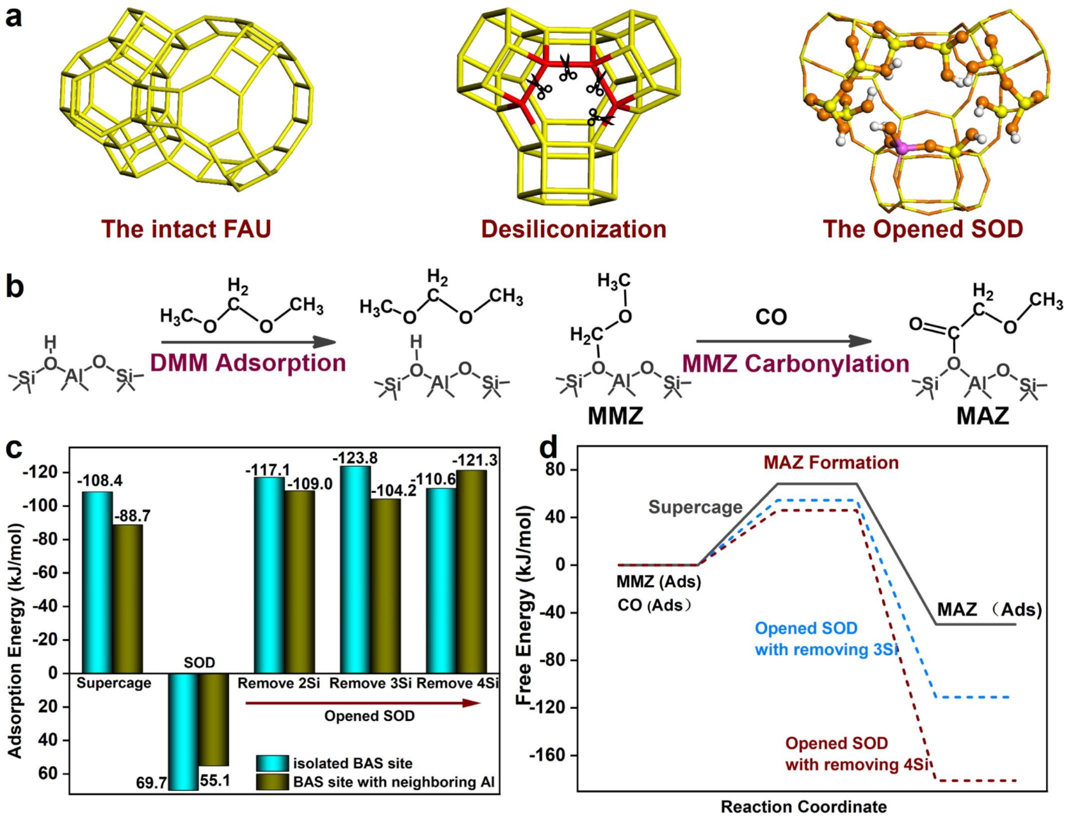

Figure 4. Theoretical calculation for the DMM adsorption and CO interaction reaction. (a) A model representing opened SOD constructed by removing Si atoms from the six-membered rings within the SOD cage. (b) DMM adsorption and CO interaction reaction process. (c) The adsorption energy of DMM on the SC, SOD, and opened SOD with isolated BAS and BAS site with neighboring Al considered (5 Al atoms per unit cell). (d) The free energy profile of the interaction of CO with methoxymethoxy groups (MMZ) for the formation of methoxyacetyl species (MAZ) in the supercage and opened SOD with removal of 3Si and 4Si.

NMR spectra in Figure 2d. Furthermore, for H-FAU-I-F, the ^{13}CO concentration within SOD cages substantially exceeds that in SC, indicating preferential accumulation of CO in the opened SOD cages. This preference persists even at higher pressures (3 atm), although adsorption peaks shift upfield (Figure S19). Given the enrichment of both DMM and CO within the opened SOD cages of H-FAU-I-F, the subsequent reaction was investigated. The reaction of adsorbed DMM and ^{13}CO over H-FAU-I-F was monitored by ^{1}H−^{13}C cross-polarization (CP) MAS NMR spectra in Figure 3d. The ^{13}CO molecular signal is negligible due to the absence of nearby ^{1}H atoms, preventing ^{1}H−^{13}C polarization transfer. Additionally, since DMM lacks isotopic labeling and disproportionation is minimal, signals for methyl formate (MF) or DME are absent. Weak peaks at 55 and 98 ppm arise from the $-OCH_3$ and $-OCH_2O-$ groups of natural abundance of ^{13}C in DMM, while the peak at 60 ppm is assigned to the $O-CH_3$ group of MMAc. Increasing temperature weakens the DMM peaks (55, 98 ppm) and strengthens the MMAc peak (60 ppm), confirming DMM consumption and MMAc formation. Analogous to DME carbonylation studies where methyl acetate adsorbed in 8-MR and 12-MR was distinctly identified by ^{13}C MAS NMR technology,[43,44] deconvolution of the C═O region in DMM carbonylation (Figure S20) reveals three peaks at 182, 177, and 171 ppm, which can be attributed to acyl species of MMAc adsorbed in SOD, SC, and the physical adsorption state, respectively. In order to identify the variation trend of the carbonyl groups in MMAc confined in different microenvironments, theoretical calculation was used to predict the ^{13}C chemical shift. Figure S21 provided the optimized structures of MMAc adsorbed in the SC and opened SOD. As shown in Table S5, the theoretical calculations of ^{13}C chemical shifts are in good agreement with the observations of ^{13}C NMR spectroscopy. The emergence of a small peak at 182 ppm at 297 K indicates carbonylation can even be initiated at room temperature. Upon heating to 393 K, the peak at 182 ppm intensifies dramatically, accompanied by weaker peaks at 177 and 171 ppm. The initial appearance of the SOD-associated peak (182 ppm) at low temperature, followed by the SC peak (177 ppm) at higher temperatures, suggests higher intrinsic activity for B@SOD sites compared to those in SC. The ^{1}H MAS NMR spectra of H-FAU-I-F before and after reaction (Figure S22a) show the disappearance of the methylenedioxy ($-OCH_2O-$) signal of DMM and the emergence of the methylenethoxy acetyl ($-OCH_2CO-$) signal of MMAc. After the reaction, 2D ^{1}H−^{13}C heteronuclear correlation (HETCOR) of H-FAU-I-F was obtained (Figure S22b), and three carbonyl species can be classified as MMAc.

Furthermore, to verify that the carbonyl signals in the ^{13}C CP MAS NMR spectrum originate from MMAc or its derivatives, MMAc was adsorbed onto the extensively opened SOD sample (H-FAU-I-F) and the partially opened SOD reference sample (H-FAU-ref) after dehydration (Figure S23). H-FAU-ref was obtained by ammonia exchange of NaY and then calcined in a tube furnace at 823 K for 6 h, which could cause slight dealuminization of the FAU zeolites according to existing literature.[45] After MMAc adsorption, H-FAU-ref exhibits a major carbonyl peak at ~172 ppm, corresponding to MMAc adsorbed within SC. Notably, H-FAU-I-F with adsorbed MMAc displays two distinct carbonyl signals at ~182 and ~172 ppm, with the ~182 ppm peak being dominant. This confirms that the ~182 ppm signal arises from MMAc adsorbed within the SOD cages, indicating preferential accumulation of MMAc in these sites.

Theoretical Calculations for Adsorption and Carbonylation in Opened SOD. Ten distinct models representing the SC, SOD, and opened SOD, considering the isolated BAS site and BAS site with neighboring Al, were constructed. The opened SOD structures were built by removing two/three/four Si atoms from the six-membered rings within the SOD cage (Figures S24 and S25). In this case, the adsorption energies of DMM in SC, SOD, and opened SOD were compared (Figure 4 and Figures S26, S27). As shown in Figure 4c, the calculated results exhibited that the adsorption energy of DMM confined in the opened SOD (−104.2 to −123.8 kJ/mol) is lower than that in the SC (−88.7 to −108.4 kJ/mol) and the intact SOD (55.1 to 69.7 kJ/mol), suggesting that the opened SOD cage could stabilize the reactant DMM, which is consistent with the results of ^{1}H MAS NMR (Figure 3b). In addition, by combining the results from the[2,9] Si MAS NMR (Figure 2e), which indicate the presence of a trace amount of neighboring Al, the effect of proximal Al was investigated in depth. As shown in Figure 4c, the adsorption energy of DMM on the BAS site with neighboring Al (−88.7 to −121.3 kJ/mol) is significantly higher by 8.1 to 19.7 kJ/mol than that on the isolated BAS site (−108.4 to −123.8 kJ/mol), suggesting the neighboring Al is unfavorable for DMM adsorption due to repulsive interactions.[19] Besides, considering that the rate-limiting step of the DMM carbonylation reaction is the process of CO insertion, the reaction energies of this step were also calculated. As shown in Figure 4d, the free energy barrier of the CO insertion reaction in the opened SOD cage with the removal of 3Si and 4Si (54.4, 45.9 kJ/mol) is lower by 13.7−22.2 kJ/mol than that in the SC (68.1 kJ/mol). The transition state of DMM carbonylation in SC and opened SOD was shown in Figure S28. The reason for the energy decline could be attributed to the stronger acid strength and the more confined space of the SOD cage. The energy feasibility of the CO insertion reaction, combined with the ^{1}H−^{13}C CP MAS NMR spectra results, reveals that the CO insertion step prefers to occur in the opened SOD cage.

CONCLUSIONS

In summary, we demonstrate that Brønsted acid sites within opened SOD cages of H-FAU zeolites predominantly catalyze DMM carbonylation. The SOD-opened H-FAU-I-F catalyst (Si/Al ≈ 6), prepared via mild NH_4F treatment, stably exhibits a 90% MMAc selectivity with an MMAc STY of 0.7 g g^{-1} h^{-1} over 500 h at 343 K, 5 MPa, and CO/DMM = 19. N_2 isotherms and HP ^{129}Xe NMR spectra confirm the accessibility of the opened SOD cages. Complementarily, IR spectra and ^{27}Al and ^{1}H MAS NMR spectra verify the increase in SOD Brønsted acid sites following EFAl species removal by NH_4F. ^{1}H MAS NMR with deuterated DMM and ^{13}C MAS NMR with ^{13}CO reveal preferential accumulation of both reactants within opened SOD cages. ^{1}H−^{13}C CP MAS NMR further confirms that carbonylation primarily occurs in these SOD sites, which is supported by theoretical calculations, indicating enhanced reactivity within opened SOD cages. These findings not only guide the design of efficient and cost-effective industrial catalysts for DMM carbonylation but also contribute to a more profound comprehension of zeolite-catalyzed Koch carbonylation reactions.

METHODS

Catalyst Preparation. The H-FAU-I and H-FAU-II zeolites were commercially provided. The H-FAU-I sample (5 g) was added into a 10% NH_4F aqueous solution (100 mL) and stirred under ultrasonic radiation at 278 K (ice bath) for 5 min. After filtration, the solid sample was washed with 100 mL of deionized water, then dried at 383 K for 30 min. The obtained solid sample was subsequently ion-exchanged twice with 1 mol/L of NH_4Cl aqueous solution (liquid/solid = 10) at 353 K for 2 h each time. The ion-exchanged sample was filtered, washed (with deionized water), dried (383 K), and finally calcined at 823 K for 4 h. The resulting sample was denoted as H-FAU-I-F. The H-FAU-II sample was treated by the same procedure as above, and the resulting sample was denoted as H-FAU-II-F. The H-FAU zeolites were pressed, crushed, and sieved to 0.4−0.8 mm before the catalytic test.

Catalytic Evaluation. The carbonylation of the DMM reaction was performed in a fixed-bed stainless-steel reactor (8 mm inner diameter). A sheathed K-type thermocouple was placed in the catalyst bed. Typically, 0.5 g of zeolite catalyst was loaded into the reactor and heated to 673 K for 2 h under 30 mL/min Ar to remove residual moisture, then cooled to the reaction temperature. DMM was introduced into the reactor by 40 mL/min CO (≥99.9%), which was passed through a stainless-steel saturator filled with DMM kept at 298 K. The reaction effluent was kept at 433 K and analyzed online by an Agilent gas chromatograph (Agilent 7890B), which was equipped with an FFAP capillary column and a flame ionization detector. The conversion and selectivity were calculated on mass with the following equations.

$$\text{DMM conversion} = (\text{DMM}_{\text{in}} - \text{DMM}_{\text{out}})/(\text{DMM}_{\text{in}}) \times 100\% \quad (1)$$

$$\text{MMAc selectivity} = \text{M}_{\text{MMAc}}/(\text{total mass of products}) \times 100\% \quad (2)$$

$$\text{DME selectivity} = \text{M}_{\text{DME}}/(\text{total mass of products}) \times 100\% \quad (3)$$

$$\text{MF selectivity} = \text{M}_{\text{MF}}/(\text{total mass of products}) \times 100\% \quad (4)$$

Note: the selectivity of other byproducts such as MeOH, DMM_2, and MMAc derivatives was calculated according to eq 2; DMM_{in}: DMM mass at the inlet; DMM_{out}: DMM mass at the outlet; M_{MMAc}: MMAc mass; M_{DME}: DME mass; M_{MF}: MF mass.

Catalyst Characterization. The XRD patterns were tested on a PANalytical X'Pert Pro diffractometer with Cu Kα radiation. The composition of the zeolites was determined on a Philips Magix-601 X-ray fluorescence (XRF) spectrometer. The morphology of the zeolite catalysts was observed on an SU8020 scanning electron microscope (SEM). A Micromeritics ASAP-2020 analyzer was applied to measure the textural properties via N_2 adsorption and desorption at 77 K. Zeolite samples were degassed at 623 K to remove the water under vacuum for 4 h before testing. The Brunauer−Emmett−

Teller (BET) model was utilized to estimate the surface area; meanwhile, the t-plot method was applied to calculate the pore volumes. The infrared spectra before and after pyridine adsorption were collected on a Bruker Tensor 27 instrument with a resolution of 2 cm^{-1}. Prior to the measurements, the zeolites were pressed into self-supporting disks (diameter = 14 mm) in the cell and pretreated with N_2 at 723 K for 20 min. The temperature was then lowered to 673, 523, and 423 K, and the infrared spectra before pyridine adsorption were recorded. When the temperature dropped to room temperature, pyridine was introduced under vacuum for 5 min. Then the temperature was raised to 423, 523, and 673 K, and the spectra were collected after vacuum desorption for 30 min at each temperature point.

All NMR experiments were carried out on a Bruker Avance NEO 500 MHz spectrometer. The Larmor frequencies for ^1H, ^{27}Al, ^{29}Si, ^{129}Xe, and ^{13}C nuclei were 500.13, 130.32, 99.35, 138.45, and 125.75 MHz, respectively. Before the ^1H MAS NMR experiment, the samples were enclosed in a quartz tube, which was connected to a vacuum system later. Subsequently, dehydration was carried out in a furnace under vacuum conditions (10^{-4} Pa) at 693 K for 12 h. The samples were encapsulated in the 3.2 mm ZrO_2 rotor in a glovebox in an Ar environment. The 1D ^1H MAS NMR spectra were obtained by a single pulse sequence with a $\pi/2$ pulse width of 3.5 μs and at least a 10-s recycle delay to make sure that all the ^1H nuclei were fully relaxed. The spinning rate was 20 kHz at room temperature. After the rotor cap was removed in the glovebox, the saturation adsorption of deuterated DMM (^2H-DMM) was carried out on the vacuum line for 1 h at room temperature. Then, the desorption of ^2H -DMM was performed at 353 K for 2 h in order to eliminate the physically adsorbed DMM. After sealing the samples in the glovebox, rotors were placed in the NMR spectrometer for testing. The testing conditions were consistent with those of samples prior to adsorption. The ^2H-DMM was synthesized from a 2:1 molar ratio of deuterated methanol and deuterated formaldehyde at 353 K with deuterated sulfuric acid as the catalyst.[46] The ^2H-DMM with 99.7% (molar fraction) purity and 98% isotopic enrichment was finally obtained by separating and purifying the liquid after the reaction. The purity was determined by gas chromatography (GC, Agilent 7890B), which was equipped with a flame ionization detector (FID) coupled to an HP-FFAP capillary column and a thermal conductivity detector (TCD) connected to a Porapak Q packed column. The ^{27}Al MAS NMR spectra were acquired using a $\pi/12$ pulse length of 0.32 μs with 512 scans. A single-pulse sequence was applied at a spinning rate of 12 kHz with a recycle delay of 1 s. Aluminum nitrate (0 ppm) was used as the chemical shift reference for ^{27}Al. For the ^{29}Si MAS NMR measurements, spectra were collected under high-power proton decoupling with 512 scans, a $\pi/2$ pulse width of 5.5 μs, and a relaxation delay of 10 s. The chemical shifts of ^{29}Si signals were referenced to kaolinite at −91.5 ppm. ^{27}Al MQ MAS NMR spectra were measured on a Bruker Avance III 600 MHz spectrometer with P1 4.2 μs, P2 1.4 μs, P3 15 μs, and a recycle delay of 0.1 s. For the 2D ^{27}Al Z-filter 3Q MAS experiments, the pulse durations were set to 4.2 and 1.4 μs for the first and second “hard” pulses and 15 μs for the third “soft” $\pi/2$ pulse. 3000 scans were accumulated for each of the 128 points in the t1 dimensions with an increment time of 50 μs and a recycle delay of 0.1 s.

Variable-temperature (VT) laser hyperpolarized (HP) ^{129}Xe NMR experiments were conducted at 139.1 MHz by using a 10 mm liquid NMR probe. Before the HP ^{129}Xe NMR experiment, the samples were dehydrated under a vacuum condition (10^{-4} Pa) at 693 K for 12 h and then loaded into a 10 mm self-made quartz NMR tube in the glovebox. The polarization of Xe atoms was carried out under a weak and uniform guiding magnetic field of 140 G generated by Helmholtz coils and a diode laser array of 120 W (BWT Beijing Ltd.). A flow of 1% Xe-1% N_2-98% He gas mixture was delivered at a rate of 300 mL/min to the sample in the detection region via a silanized PTFE tube. The samples were first cooled down to 143 K, and then the temperature was elevated to the desired values and kept at each temperature for 5−30 min. The spectra were recorded twice to make sure that adsorption equilibrium was reached. All one-dimensional spectra were acquired with a $\pi/2$ pulse of 11.0 μs, 512 scans, and a 0.5 s recycle delay. The chemical shifts were referenced to the signal of the xenon gas [$\delta(^{129}Xe) = 0$ ppm].

In the ^{13}C MAS NMR experiment, the samples were dehydrated under a vacuum condition (10^{-4} Pa) at 693 K for 12 h. Then, the rotors containing the samples were subsequently flushed into 1 and 3 atm ^{13}CO. ^{13}C hpdec NMR spectra were gathered with a $\pi/2$ pulse length of 4.8 μs at 100 W, a recycle delay of 10 s, and a spinning rate of 12 kHz. The chemical shifts were referenced to adamantane with the upfield methine peak at 29.5 ppm. For the *in situ* ^{13}C ss-NMR reaction experiment of DMM carbonylation, the dehydrated sample was encapsulated in the rotor that could withstand high pressure and temperature, and then DMM and 3 atm ^{13}CO were flushed into the rotor. The ^{13}C CP and hpdec MAS NMR spectra were obtained from room temperature to 393 K. The sampling condition of ^{13}C hpdec were as follows: spinning sate of 8 kHz, $\pi/2$ pulse length of 4.8 μs, a recycle delay of 10 s, scanning times of 32. In addition, ^{13}C CP MAS NMR spectra were also performed at a spinning rate of 8 kHz with contact time of 3 ms, $\pi/2$ pulse length of 4.8 μs for ^1H, and the radio field strength of ^{13}C was 48 kHz during contact. In the variable temperature experiment, nitrogen was used as a bearing gas and also used to adjust the reaction temperature.

Deuterated Dimethoxymethane Synthesis. Deuterated dimethoxymethane (D-DMM) was synthesized through a polycondensation reaction between deuterated methanol (CD_3OD) and formaldehyde (DCDO), facilitated by deuterated sulfuric acid (D_2SO_4) as the catalyst at 353 K under atmospheric pressure. The reaction was conducted in a round-bottomed flask with a methanol-to-formaldehyde molar ratio of approximately 2:1, as represented by the following equation:

$$2CD_3OD + DCDO \xrightarrow{D_2SO_4} CD_3OCD_2OCD_3 + D_2O$$

The crude product was subsequently purified. First, distillation was employed to separate D-DMM from the acidic catalyst. The resulting distillate was then treated with 4 Å molecular sieves to adsorb residual small molecules, such as water and methanol, via physical adsorption. This procedure ultimately yielded high-purity deuterated dimethoxymethane (D-DMM).

Theoretical Calculations. *DFT Calculations for the DMM Adsorption and CO Interaction Reaction.* Density functional theory (DFT) calculations were performed to validate the DMM adsorption and the CO interaction reaction. Vienna Ab initio Simulation Package (VASP)[47] was carried out for geometry optimization and transition state location using the

PBE exchange-correlation functional.[48] A rhombohedral unit cell ($Si_{43}O_{96}$) was employed for the construction of ten distinct structural models representing the SC, SOD, and opened SOD frameworks. These models were designed to feature both isolated Brønsted acid sites (BAS) and BAS sites with neighboring Al atoms with five Al substitutions per unit cell. The cell parameters were initially optimized ($a = b = c = 17.21$ Å, $\alpha = \beta = \gamma = 60°$). The opened SOD structures were built by removing two/three/four Si atoms from the six-membered rings within the SOD cage.

Grimme-type D3 corrections (DFT-D3)[49] with Becke−Johnson damping were used to consider the dispersion interaction. A plane-wave basis set with a kinetic energy cutoff of 450 eV was used. The convergence criteria were 1.0×10^{-5} eV for the SCF energy and 0.05 eV/Å for atomic force, respectively. The transition states were located by the climbing image nudged elastic band (CI-NEB) method.[50]

The adsorption energy of adsorbed (DMM) species is defined as follows:

$$\Delta E = E_{\text{Zeolite-adsorbed Species}} - E_{\text{Zeolite}} - E_{\text{adsorbed Species}}$$

Herein, $E_{\text{Zeolite-adsorbed Species}}$, E_{Zeolite}, and $E_{\text{adsorbed Species}}$ represent the energy of the system with interaction between adsorbed species and the zeolite framework, the energy of adsorbed species, and the energy of the zeolite framework, respectively.

Theoretical Calculation for ^{13}C Chemical Shifts. The structure optimization was explored by the generalized gradient approximation (GGA) proposed by Perdew, Burke, and Ernzerhof (PBE method).[48] The couplings between the core and valence electrons were described by ultrasoft pseudopotentials. A plane-wave cutoff energy of 450 eV was adopted to sample the Brillouin zone. Subsequently, based on the optimized structures, the CASTEP-NMR module in the Materials Studio package[51] was employed to calculate all NMR parameters by the GIPAW method[52] using a 2 × 2 × 2 Monkhorst−Pack K-point grid and expanding all wave functions in a plane-wave basis set at a definite cutoff energy of 500 eV. The ^{13}C-calculated chemical shift was further converted to $(\delta^{13}C)_{cal}$ values, which were referred to the absolute shielding of benzene, namely, 127 ppm for the experimental values.

ASSOCIATED CONTENT

Supporting Information

The Supporting Information is available free of charge at https://pubs.acs.org/doi/10.1021/jacs.5c13217.

Experimental procedures (catalysts preparation, catalysts tests, and characterization) and theoretical calculations; supplementary figures (XRD, pyridine-infrared spectra, IGA, HP ^{129}Xe NMR) and tables (comparison of the performance of existing catalysts, 27Al MQ NMR parameters, physicochemical properties of H-FAU zeolite, NMR analysis) (PDF)

AUTHOR INFORMATION

Corresponding Authors

Shutao Xu − *National Engineering Laboratory for Methanol to Olefins, Dalian National Laboratory for Clean Energy, National Engineering Research Center of Lower-Carbon Catalysis Technology, Dalian Institute of Chemical Physics, Chinese Academy of Sciences, Dalian 116023, P. R. China; State Key Laboratory of Catalysis, Dalian Institute of Chemical Physics, Chinese Academy of Sciences, Dalian 116023, P. R. China; University of Chinese Academy of Sciences, Beijing 100049, P. R. China;* orcid.org/0000-0003-4722-8371; Email: xushutao@dicp.ac.cn

Wenliang Zhu − *National Engineering Laboratory for Methanol to Olefins, Dalian National Laboratory for Clean Energy, National Engineering Research Center of Lower-Carbon Catalysis Technology, Dalian Institute of Chemical Physics, Chinese Academy of Sciences, Dalian 116023, P. R. China; State Key Laboratory of Catalysis, Dalian Institute of Chemical Physics, Chinese Academy of Sciences, Dalian 116023, P. R. China; University of Chinese Academy of Sciences, Beijing 100049, P. R. China;* orcid.org/0000-0002-2247-6849; Email: wlzhu@ dicp.ac.cn

Authors

Youming Ni − *National Engineering Laboratory for Methanol to Olefins, Dalian National Laboratory for Clean Energy, National Engineering Research Center of Lower-Carbon Catalysis Technology, Dalian Institute of Chemical Physics, Chinese Academy of Sciences, Dalian 116023, P. R. China; State Key Laboratory of Catalysis, Dalian Institute of Chemical Physics, Chinese Academy of Sciences, Dalian 116023, P. R. China; University of Chinese Academy of Sciences, Beijing 100049, P. R. China;* orcid.org/0000-0001-5798-9866

Xingwang Gong − *National Engineering Laboratory for Methanol to Olefins, Dalian National Laboratory for Clean Energy, National Engineering Research Center of Lower-Carbon Catalysis Technology, Dalian Institute of Chemical Physics, Chinese Academy of Sciences, Dalian 116023, P. R. China; State Key Laboratory of Catalysis, Dalian Institute of Chemical Physics, Chinese Academy of Sciences, Dalian 116023, P. R. China; University of Chinese Academy of Sciences, Beijing 100049, P. R. China*

Wenna Zhang − *National Engineering Laboratory for Methanol to Olefins, Dalian National Laboratory for Clean Energy, National Engineering Research Center of Lower-Carbon Catalysis Technology, Dalian Institute of Chemical Physics, Chinese Academy of Sciences, Dalian 116023, P. R. China; State Key Laboratory of Catalysis, Dalian Institute of Chemical Physics, Chinese Academy of Sciences, Dalian 116023, P. R. China; University of Chinese Academy of Sciences, Beijing 100049, P. R. China*

Hua Li − *National Engineering Laboratory for Methanol to Olefins, Dalian National Laboratory for Clean Energy, National Engineering Research Center of Lower-Carbon Catalysis Technology, Dalian Institute of Chemical Physics, Chinese Academy of Sciences, Dalian 116023, P. R. China; State Key Laboratory of Catalysis, Dalian Institute of Chemical Physics, Chinese Academy of Sciences, Dalian 116023, P. R. China; University of Chinese Academy of Sciences, Beijing 100049, P. R. China*

Yingying Sheng − *National Engineering Laboratory for Methanol to Olefins, Dalian National Laboratory for Clean Energy, National Engineering Research Center of Lower-Carbon Catalysis Technology, Dalian Institute of Chemical Physics, Chinese Academy of Sciences, Dalian 116023, P. R. China; State Key Laboratory of Catalysis, Dalian Institute of Chemical Physics, Chinese Academy of Sciences, Dalian 116023, P. R. China; State Key Laboratory of Fine*

Chemicals, School of Chemical Engineering, Dalian University of Technology, Dalian 116024, P. R. China

Yingxu Wei − *National Engineering Laboratory for Methanol to Olefins, Dalian National Laboratory for Clean Energy, National Engineering Research Center of Lower-Carbon Catalysis Technology, Dalian Institute of Chemical Physics, Chinese Academy of Sciences, Dalian 116023, P. R. China; State Key Laboratory of Catalysis, Dalian Institute of Chemical Physics, Chinese Academy of Sciences, Dalian 116023, P. R. China; University of Chinese Academy of Sciences, Beijing 100049, P. R. China;* orcid.org/0000-0002-0412-1980

Zhongmin Liu − *National Engineering Laboratory for Methanol to Olefins, Dalian National Laboratory for Clean Energy, National Engineering Research Center of Lower-Carbon Catalysis Technology, Dalian Institute of Chemical Physics, Chinese Academy of Sciences, Dalian 116023, P. R. China; State Key Laboratory of Catalysis, Dalian Institute of Chemical Physics, Chinese Academy of Sciences, Dalian 116023, P. R. China; University of Chinese Academy of Sciences, Beijing 100049, P. R. China;* orcid.org/0000-0002-7999-2940

Complete contact information is available at:
https://pubs.acs.org/10.1021/jacs.5c13217

Author Contributions

#Y.N., X.G., and W.Z. contributed equally to this work.

Notes

The authors declare no competing financial interest.

■ ACKNOWLEDGMENTS

We acknowledge the financial support from the National Natural Science Foundation of China (Grant Nos. 22378388, 22241801, 22288101, 22372169); the Dalian Outstanding Young Scientist Foundation (2021RJ01); and the Liaoning International Joint Laboratory Project (2024JH2/102100005). This study is supported by the Clean Combustion and Low-Carbon Utilization of Coal, Strategic Priority Research Program of the Chinese Academy of Sciences, Grant No. XDA29030400. We thank Weichen Zhang for assistance in the experiments.

■ REFERENCES

(1) Aresta, M.; Dibenedetto, A.; Angelini, A. Catalysis for the valorization of exhaust carbon: from CO_2 to chemicals, materials, and fuels. Technological use of CO_2. *Chem. Rev.* **2014**, *114*, 1709−1742.

(2) Shi, C.; Quinn, E. C.; Diment, W. T.; Chen, E. Y. X. Recyclable and (bio)degradable polyesters in a circular plastics economy. *Chem. Rev.* **2024**, *124*, 4393−4478.

(3) Centi, G.; Quadrelli, E. A.; Perathoner, S. Catalysis for CO_2 conversion: a key technology for rapid introduction of renewable energy in the value chain of chemical industries. *Energy Environ. Sci.* **2013**, *6*, 1711−1731.

(4) Celik, F. E.; Kim, T.; Mlinar, A. N.; Bell, A. T. An investigation into the mechanism and kinetics of dimethoxymethane carbonylation over FAU and MFI zeolites. *J. Catal.* **2010**, *274*, 150−162.

(5) Sheikh, K. A.; Francesconi, V. Z.; Zevaco, T. A.; Sauer, J. Carbonylation of dimethoxymethane: a study on the reactivity of different solid acid catalysts. *Catal. Sci. Technol.* **2024**, *14* (5), 1148−1166.

(6) Yao, J.; Shi, L.; Deng, W.; Fan, J.; Wang, Y.; Gao, W.; Zhang, D.; Zhu, W.; Liu, Z. Facile Sulfolane-Modified Resins for Enhanced Dimethoxymethane Carbonylation. *Catal. Sci. Technol.* **2020**, *10*, 2561−2572.

(7) DICP *Technical Development Progress Of "Methyl Glycolate Production Via Dimethoxymethane Carbonylation And Hydrolysis From Methyl Methoxyacetate"*. https://dicp.cas.cn/xwdt/kyjz/202212/t20221202_6565978.html

(8) Samantaray, P. K.; Little, A.; Haddleton, D. M.; McNally, T.; Tan, B.; Sun, Z.; Huang, W.; Ji, Y.; Wan, C. Poly(glycolic acid) (PGA): A Versatile Building Block Expanding High Performance and Sustainable Bioplastic Applications. *Green Chem.* **2020**, *22*, 4055−4081.

(9) Liu, S.; Zhu, W.; Shi, L.; Liu, H.; Liu, Y.; Ni, Y.; Li, L.; Zhou, H.; Xu, S.; He, Y.; Liu, Z. Activity Enhancement of Nafion Resin: Vapor-Phase Carbonylation of Dimethoxymethane over Nafion-Silica Composite. *Appl. Catal., A* **2015**, *497*, 153−159.

(10) Wang, J. P.; Liu, J. H.; Song, H. Y.; Chen, J. Heteropolyacids as efficient catalysts for the synthesis of precursors to ethylene glycol by the liquid-phase carbonylation of dimethoxymethane. *Chem. Lett.* **2015**, *44*, 806−808.

(11) Xie, Z.; Chen, C.; Hou, B.; Sun, D.; Guo, H.; Wang, J.; Li, D.; Jia, L. Study of the Nature of High-Silica H−Y Acid Sites in Dimethoxymethane Carbonylation by NH_3 Poisoning. *J. Phys. Chem. C* **2018**, *22*, 9909−9917.

(12) Zhang, D.; Shi, L.; Wang, Y.; Chen, F.; Yao, J.; Li, X.; Ni, Y.; Zhu, W.; Liu, Z. Effect of Mass-Transfer Control on HY Zeolites for Dimethoxymethane Carbonylation to Methyl Methoxyacetate. *Catal. Today* **2018**, *316*, 114−121.

(13) Wu, J.; Zhang, X.; Sun, Z.; Li, H.; Zhou, W.; Zhao, Y. Effect of NaOH Content in the Synthesis Gel on the Catalytic Performance of H-ZSM-5 Zeolites in the Gas Phase Carbonylation of Dimethoxymethane. *J. Fuel Chem. Technol.* **2019**, *47*, 1226−1234.

(14) Cheung, P.; Bhan, A.; Sunley, G. J.; Iglesia, E. Selective carbonylation of dimethyl ether to methyl acetate catalyzed by acidic zeolites. *Angew. Chem., Int. Ed.* **2006**, *45*, 1617−1620.

(15) Bhan, A.; Allian, A. D.; Sunley, G. J.; Law, D. J.; Iglesia, E. Specificity of Sites within Eight-Membered Ring Zeolite Channels for Carbonylation of Methyls to Acetyls. *J. Am. Chem. Soc.* **2007**, *129*, 4919−4924.

(16) Boronat, M.; Martinez-Sanchez, C.; Law, D.; Corma, A. Enzyme-like specificity in zeolites: A unique site position in mordenite for selective carbonylation of methanol and dimethyl ether with CO. *J. Am. Chem. Soc.* **2008**, *130*, 16316−16323.

(17) Celik, F. E.; Kim, T. J.; Bell, A. T. Vapor-phase carbonylation of dimethoxymethane over H-faujasite. *Angew. Chem., Int. Ed.* **2009**, *48*, 4813−4815.

(18) Shapovalov, V.; Bell, A. T. Theoretical study of zeolite-catalyzed dimethoxymethane carbonylation to methyl methoxyacetate. *J. Phys. Chem. C* **2010**, *114*, 17753−17760.

(19) Celik, F. E.; Kim, T. J.; Bell, A. T. Effect of zeolite framework type and Si/Al ratio on dimethoxymethane carbonylation. *J. Catal* **2010**, *270*, 185−195.

(20) Qin, Z.; Cychosz, K. A.; Melinte, G.; El Siblani, H.; Gilson, J.-P.; Thommes, M.; Fernandez, C.; Mintova, S.; Ersen, O.; Valtchev, V. Opening the Cages of Faujasite-Type Zeolite. *J. Am. Chem. Soc.* **2017**, *139*, 17273−17276.

(21) Lakiss, L.; Kouvatas, C.; Gilson, J. P.; Aleksandrov, H. A.; Vayssilov, G. N.; Nesterenko, N.; Mintova, S.; Valtchev, V. Unlocking the Potential of Hidden Sites in Faujasite: New Insights in a Proton Transfer Mechanism. *Angew. Chem., Int. Ed.* **2021**, *60*, 26702−26709.

(22) Li, X.; Han, H.; Xu, W.; Hwang, S.-J.; Lu, P.; Bhan, A.; Tsapatsis, M. Enhanced Reactivity of Accessible Protons in Sodalite Cages of Faujasite Zeolite. *Angew. Chem., Int. Ed.* **2022**, *61*, No. e202111180.

(23) Ni, Y.; Zhu, W.; Liu, Z. H-ZSM-5-Catalyzed hydroacylation involved in the coupling of methanol and formaldehyde to aromatics. *ACS Catal.* **2019**, *9*, 11398−11403.

(24) Yang, L.; Ni, Y.; Xie, M.; Chen, Z.; Fang, X.; Li, B.; Liu, H.; Zhu, W. A Green and Moderate Approach for the Synthesis of Methyl Formate via Dimethoxymethane Disproportionation over H-Zeolites. *Appl. Catal., A* **2024**, *683*, 119860.

(25) Yao, J.; Wang, Y.; Bello, S. S.; Xu, G.; Shi, L. Regulation of Brønsted Acid Sites in H-MOR for Selective Methyl Methoxyacetate Synthesis. *Appl. Organomet. Chem.* **2020**, *34* (11), No. e5925.

(26) Chen, F.; Zhang, D.; Shi, L.; Wang, Y.; Xu, G. Optimized pore structures of hierarchical HY zeolites for highly selective production of methyl methoxyacetate. *Catalysts* **2019**, *9*, 865.

(27) Gao, S.; Lu, P.; Qi, L.; Wang, Y.; Li, H.; Ye, M.; Valtchev, V.; Bell, A. T.; Liu, Z. Dimethoxymethane Carbonylation and Disproportionation over Extra-Large Pore Zeolite ZEO-1: Reaction Network and Mechanism. *Chin. J. Catal.* **2025**, *68*, 230−245.

(28) Xu, B.; Bordiga, S.; Prins, R.; van Bokhoven, J. A. Effect of framework Si/Al ratio and extra-framework aluminum on the catalytic activity of Y zeolite. *Appl. Catal. A* **2007**, *333*, 245−253.

(29) Li, X.; Han, H.; Xu, W.; Hwang, S.-J.; Lu, P.; Bhan, A.; Tsapatsis, M. Acid Catalysis over Low-Silica Faujasite Zeolites. *J. Am. Chem. Soc.* **2022**, *144*, 9324−9329.

(30) Van Bokhoven, J. A.; Roest, A. L.; Koningsberger, D. C.; Miller, J. T.; Nachtegaal, G. H.; Kentgens, A. P. M. Changes in Structural and Electronic Properties of the Zeolite Framework Induced by Extraframework Al and La in H-USY and La(x)NaY: A ^{29}Si and ^{27}Al MAS NMR and ^{27}Al MQ MAS NMR Study. *J. Phys. Chem. B* **2000**, *104* (29), 6743−6754.

(31) Chen, K.; Horstmeier, S.; Nguyen, V. T.; Wang, B.; Crossley, S. P.; Pham, T.; Gan, Z.; Hung, I.; White, J. L. Structure and Catalytic Characterization of a Second Framework Al(IV) Site in Zeolite Catalysts Revealed by NMR at 35.2 T. *J. Am. Chem. Soc.* **2020**, *142*, 7514−7523.

(32) Katsiotis, M. S.; Fardis, M.; Al Wahedi, Y.; Stephen, S.; Tzitzios, V.; Boukos, N.; Kim, H. J.; Alhassan, S. M.; Papavassiliou, G. Water Coordination, Proton Mobility, and Lewis Acidity in HY Nano-zeolites: A High-Temperature 1H and 27Al NMR Study. *J. Phys. Chem. C* **2015**, *119*, 3428−3438.

(33) Engelhardt, G.; Kentgens, A. P. M.; Koller, H.; Samoson, A. Strategies for extracting NMR parameters from ^{23}Na MAS, DOR and MQMAS spectra. A case study for $Na_4P_2O_7$. *Solid State Nucl. Magn. Reson.* **1999**, *15*, 171−180.

(34) Gil, B.; Zones, S. I.; Hwang, S.-J.; Bejblová, M.; Čejka, J. Acidic Properties of SSZ-33 and SSZ-35 Novel Zeolites: A Complex Infrared and MAS NMR Study. *J. Am. Chem. Soc.* **2008**, *112*, 2997−3007.

(35) Ravi, M.; Sushkevich, V. L.; van Bokhoven, J. A. On the Location of Lewis Acidic Aluminum in Zeolite Mordenite and the Role of Framework-Associated Aluminum in Mediating the Switch between Brønsted and Lewis Acidity. *Chem. Sci.* **2021**, *12*, 4094−4103.

(36) Ravi, M.; Sushkevich, V. L.; van Bokhoven, J. A. Towards a Better Understanding of Lewis Acidic Aluminium in Zeolites. *Nat. Mater.* **2020**, *19*, 1047−1056.

(37) Haouas, M.; Kogelbauer, A.; Prins, R. The Effect of Flexible Lattice Aluminium in Zeolite Beta during the Nitration of Toluene with Nitric Acid and Acetic Anhydride. *Catal. Lett.* **2000**, *70*, 61−65.

(38) Giudici, R.; Kouwenhoven, H. W.; Prins, R. Comparison of Nitric and Oxalic Acid in the Dealumination of Mordenite. *Appl. Catal., A* **2000**, *203*, 101−110.

(39) Gola, A.; Rebours, B.; Milazzo, E.; Lynch, J.; Benazzi, E.; Lacombe, S.; Delevoye, L.; Fernandez, C. Effect of Leaching Agent in the Dealumination of Stabilized Y Zeolites. *Microporous Mesoporous Mater.* **2000**, *40*, 73−83.

(40) Qin, Z.; Zeng, S.; Melinte, G.; Bučko, T.; Badawi, M.; Shen, Y.; Gilson, J.-P.; Ersen, O.; Wei, Y.; Liu, Z.; et al. Understanding the Fundamentals of Microporosity Upgrading in Zeolites: Increasing Diffusion and Catalytic Performances. *Adv. Sci.* **2021**, *8* (17), 2100001.

(41) Li, S.; Zheng, A.; Su, Y.; Zhang, H.; Chen, L.; Yang, J.; Ye, C.; Deng, F. Brønsted/Lewis Acid Synergy in Dealuminated HY Zeolite: A Combined Solid-State NMR and Theoretical Calculation Study. *J. Am. Chem. Soc.* **2007**, *129*, 11161−11171.

(42) Mezari, B.; Magusin, P. C. M. M.; Almutairi, S. M. T.; Pidko, E. A.; Hensen, E. J. M. Nature of Enhanced Brønsted Acidity Induced by Extraframework Aluminum in an Ultrastabilized Faujasite Zeolite: An In Situ NMR Study. *J. Phys. Chem. C* **2021**, *125*, 9050−9059.

(43) Li, B.; Xu, J.; Han, B.; Wang, X.; Qi, G.; Zhang, Z.; Wang, C.; Deng, F. Insight into Dimethyl Ether Carbonylation Reaction over Mordenite Zeolite from in Situ Solid-State NMR Spectroscopy. *J. Phys. Chem. C* **2013**, *117*, 5840−5847.

(44) He, T.; Ren, P.; Liu, X.; Xu, S.; Han, X.; Bao, X. Direct Observation of DME Carbonylation in the Different Channels of H-MOR Zeolite by Continuous-Flow Solid-State NMR Spectroscopy. *Chem. Commun.* **2015**, *51*, 16868−16870.

(45) Zornes, A.; Abdul Rahman, N. B.; Das, O. R.; Gomez, L. A.; Crossley, S.; Resasco, D. E.; White, J. L. Impact of Low-Temperature Water Exposure and Removal on Zeolite HY. *J. Am. Chem. Soc.* **2024**, *146*, 1132−1143.

(46) Ren, J.; Xin, F.; Xu, Y. A Review on Direct Synthesis of Dimethoxymethane. *Chin. J. Chem. Eng.* **2022**, *50*, 43−55.

(47) Kresse, G.; Furthmüller, J. Efficient Iterative Schemes for Ab Initio Total-Energy Calculations Using a Plane-Wave Basis Set. *Phys. Rev. B* **1996**, *54*, 11169−11186.

(48) Perdew, J. P.; Burke, K.; Ernzerhof, M. Generalized Gradient Approximation Made Simple. *Phys. Rev. Lett.* **1996**, *77*, 3865−3868.

(49) Grimme, S.; Antony, J.; Ehrlich, S.; Krieg, H. A Consistent and Accurate Ab Initio Parametrization of Density Functional Dispersion Correction (DFT-D) for the 94 Elements H-Pu. *J. Chem. Phys.* **2010**, *132*, 154104.

(50) Henkelman, G.; Uberuaga, B. P.; Jónsson, H. A Climbing Image Nudged Elastic Band Method for Finding Saddle Points and Minimum Energy Paths. *J. Chem. Phys.* **2000**, *113*, 9901−9904.

(51) *Materials Studio 6.0*; Accelrys Inc.: San Diego, CA, 2012.

(52) Profeta, M.; Mauri, F.; Pickard, C. J. Accurate First Principles Prediction of ^{17}O NMR Parameters in SiO_2: Assignment of the Zeolite Ferrierite Spectrum. *J. Am. Chem. Soc.* **2003**, *125*, 541−548.